

# Research on the Hoisting Motor Drive System's Active Disturbance Rejection Control and Energy Consumption for a Crane

ZHONG BIN<sup>1</sup>, MA LILI<sup>2</sup>, DONG HAO<sup>1</sup>, AND REN ZHENXING<sup>1</sup>

<sup>1</sup>School of Mechanical Engineering, Chengdu University, Chengdu 610106, China

<sup>2</sup>College of Equipment Management and Support, Engineering University of PAP, Xi'an 710086, China

Corresponding author: Zhong Bin (zhongbinchina@163.com)

This work was supported by the National Natural Science Foundation of China under Grant 11802041.

**ABSTRACT** To allow the hoisting motor drive system of a crane to track a load torque quickly, a linearization method was used to transform a motor nominal dynamics model into two decoupled linear rotor speed and flux linkage subsystems. The method based on the theory of differential geometry was a precise feedback method. Two active disturbance rejection controllers (ADRCs) with identical structures were designed for the rotor speed and flux linkage subsystems. The extended state observer of the ADRC could estimate the unmodeled dynamics of the motor, the variation of motor parameters due to heating, and the unknown disturbances of the motor system to determine the total disturbances of the system. A closed-loop system with ADRC and an open-loop system were compared. The motor's full-load starting time was reduced by about 50%. When the motor operated smoothly at different load rates and the rated load was suddenly applied, the electromagnetic torque fluctuation range did not exceed 20 N · m. The rotor flux was always stable at the reference value. The motor speed decreased, but the amount of decrease did not exceed 7 rad/s. The closed-loop system had a significant energy-saving effect during the motor's starting process. The power saving rate was about 55%–59% if the motor started with a light load. The power saving rate could reach 71% if the motor started with a heavy load. The ADRC system could accurately estimate the unknown model of the rotor speed and flux linkage subsystems, and adapt to parameter variations of the motor stator and rotor resistance in the range of ±10%.

**INDEX TERMS** Crane, hoisting motor drive system, active distance rejection control, energy consumption, energy-saving control.

## NOMENCLATURE

*Multi-Input Multi-Output (MIMO) Affine Nonlinear System:*

$x, u, y$	State variables, input and output vectors.
$f(x), g(x)$	Sufficiently smooth vector fields.
$g_j(x)$	The $j$ -th column vector.
$f_j(x)$	The $j$ -th scalar function.
$h_j(x)$	The $j$ -th output function.
$\gamma$	Relative order vector.
$\gamma_j$	The $j$ -th relative order number.

*Motor Drive System of Lifting Mechanism for the Crane:*

$J_e, J_1, J_2, J_r$	Moments of inertia.
$n_1, n_2, n_r$	Rotational speeds.
$j_1, j_2, j_r$	Reduction ratios.
$\eta_1, \eta_2, \eta_r, \eta_L$	Transmission efficiencies.
$D$	Diameter of the lifting drum.
$m_L$	Payload.
$m_0$	Quality of the hook.
$F_L$	Wire rope's static tension.
$g$	Gravitational acceleration.

*Motor:*

$T_e, T_L$	Electromagnetic and load torques.
$T_N$	Nominal torque.

The associate editor coordinating the review of this manuscript and approving it for publication was Choon Ki Ahn<sup>1</sup>.

$E_T$	Electromagnetic torque tracking error.
$n_p$	Motor's pole logarithm.
$J_e$	Rotational inertia of the rotor.
$n$	Rotor speed.
$\omega$	Electric angular velocity.
$\omega_r$	Mechanical angular velocity.
$\alpha, \beta$	Static two-phase coordinate axis.
A, B, C	Three-phase coordinate axis.
$u_{s\alpha}, u_{s\beta}, u_{r\alpha}, u_{r\beta}$	Stator and rotor voltages in $\alpha$ - $\beta$ coordinate system.
$i_{s\alpha}, i_{s\beta}, i_{r\alpha}, i_{r\beta}$	Stator and rotor currents in $\alpha$ - $\beta$ coordinate system.
$\psi_{s\alpha}, \psi_{s\beta}, \psi_{r\alpha}, \psi_{r\beta}$	Stator and rotor flux linkages.
$R_s, R_r$	Stator and rotor resistances.
$L_s, L_r, L_m$	Stator, rotor and mutual inductances.
$u_A^*, u_B^*, u_C^*$	PWM's three-phase modulation voltages.
$u_A, u_B, u_C$	Motor's three-phase control voltages.
$I(t), U(t), P(t)$	Effective value of the stator current, voltage and power.
$W_{sk}, W_{sb}$	Starting energy consumption.
$t_s$	Starting time.
$\Delta E$	Power saving rate.
<b>ADRC:</b>	
$\beta^{(ESO)}, \beta^{(ENC)}$	Parameter vector of ADRC.
$e^{(TD)}, e^{(ESO)}, e_1^{(ENC)}, e_2^{(ENC)}$	Tracking error.
$w_1, w_2$	TD's outputs.
$z_1, z_2, z_3$	State variables, and expanded state variable.
$\hat{z}_1, \hat{z}_2, \hat{z}_3$	Estimated state variables.
$b$	Compensation factor of the control strength.
$T$	Integral step.
$r$	Speed factor.
$v_1, v_2$	Virtual control input.
$y_1^*, y_2^*$	Reference input.

**I. INTRODUCTION**

A crane is an important type of logistics equipment to realize material handling mechanization in factory workshops or warehouses, railway freight yards, port wharfs, and other locations [1], [2]. Three phase AC (alternating current) asynchronous motors (hereinafter referred to as motors) serve as the main power devices for a crane's cart running mechanism, trolley running mechanism, and spout lifting mechanism [3], [4]. The motor and drive system of the running or lifting mechanism constitute the motor drive system of the crane. In the life cycle of the crane, 97%–98% of the operating cost is used to maintain the electric charge of the crane motor drive system [5], [6]. Thus, effective control of the crane motor drive system is an important means to improve the crane automation level, energy consumption, and crane operation efficiency [7], [8].

Crane systems mainly include a cart motor drive system, trolley motor drive system and a hoisting (lifting) motor drive system. As a main factor of improvement in the energetic efficiency of the crane, particular attention should be paid on the hoisting motor drive system [9]. For the crane hoisting motor drive system, Chen *et al.* [10] proposed an energy loss system, derived the calculation formula of the energy recovery late, and developed the control strategy of the energy-saving system. But Chen's research was based on the mechanical connection with the winch-motor-synchronous motor. The hoisting motor drive system has the distinct characteristics of a continually applied torque and variable working conditions [11], [12]. The load torque is a braking torque that hinders the movement, and the braking torque includes the continually applied torque of the driving wheel resistance of the cart or trolley and the torque from the potential energy of the lifting reel [13]. For the crane's lifting motor drive system, the load torque is often uncertain, due to the variability of the load. Therefore, the energy-saving principles and control measures adopted for the crane motor drive system are different from those of a motor drive system with a constant power load, such as a fan or pump [14].

In general, there are three kinds of energy-saving control and implementation measures of a motor drive system. The first requires optimization of the motor's internal structure and its magnetic material selection [15]. Reducing the copper and iron losses from the stator and rotor windings reduces internal losses of the motor [16], [17]. The second utilizes control strategies based on the steady-state operation of the motor. The third involves vector control based on a dynamic mathematical model of the motor to realize real-time control of the motor's electromagnetic torque [18]–[20].

Steady-state control strategies include variable voltage speed regulation, variable pole speed regulation, and variable frequency speed regulation. Energy feedback utilization technology is needed to utilize the slip energy in the variable voltage speed regulation process, and the motor power factor is low. The variable pole speed regulation cannot achieve stepless speed regulation smoothly, and the speed regulation range is limited because of the motor structure and manufacturing technology. Variable frequency speed regulation exhibits no additional slip loss, a high efficiency, and a wide speed range, and it is especially suitable for operating under low loads most of the times, which is the typical operating condition of a crane, and for frequent starting and stopping operations [21], [22].

Vector control theories and methods mainly include adaptive control [23]–[25], back stepping control [26], inverse dynamic control [27], passive control [28], sliding mode control [29], [30], and fuzzy logic control [31], [32]. Owing to the coupling terms of the state variables in the motor dynamics equations, the torque and excitation components of the motor stator current influence each other, and affect the dynamic performance of the control system. The control methods described previously require complex controller design [23]–[32], and they cannot influence the decoupled

control of the output variables. In addition, when motor parameters (e.g., self-inductance) change due to factors such as temperature rise, the control system's performance may suffer. The uncertainty of the load rate also creates higher requirements for the controller design [33], [34]. If the motor's dynamic model can be decoupled while devising an equivalently simple model of the motor, the controller design will be straightforward.

For affine nonlinear systems, such as motors [35], [36], the nonlinear systems can be linearized using the method of state variable feedback, which is a nonlinear feedback linearization method based on the theory of differential geometry [37]. Unlike local linear approximations using Taylor series expansions, nonlinear feedback linearization does not ignore any higher-order nonlinear terms in the linearization process, so the linearization is accurate and global. Using this nonlinear feedback linearization method, the coupled and complex nonlinear control system of an AC induction motor is transformed into two completely decoupled and simple second-order subsystems: linear rotor speed and flux linkage. On this basis, the complete decoupling control of these subsystems can be realized. This decoupling control is based on the premise that the motor has an accurate mathematical model. However, the motor parameters and the crane's load torque often have some a degree of uncertainty. In addition, the model does not account for all the dynamics in the system, leading to inaccuracies in the system dynamics model, resulting in a nominal dynamic model of the motor.

The active disturbance rejection control (ADRC) theory and methods do not rely heavily on the controlled object's mathematical model [38], [39], so the ADRC can solve the control problem of uncertainty well [40]–[42]. Sun *et al.* [43] used the ADRC method to control the open cathode proton exchange membrane fuel cell. Deng *et al.* [44] researched a vector control strategy of the permanent magnet synchronous motor based on ADRC technology. Patelski *et al.* [45] designed an ADRC controller for uncertain robot hand models. Zhonghua [46] detailed how an ADRC was applied to the naval gun servo system. Huang *et al.* [47] explored a self-searching optimal ADRC for the pitch angle control of an underwater thermal glider under vertical plane motion. Xie *et al.* [48] applied an ADRC to solve the speed fluctuation problem of permanent magnet synchronous motors resulting from parameter variation and load disturbance. Lotufo *et al.* [49] used an ADRC for UAV attitude control. Li *et al.* [50] designed an ADRC for the path following of underactuated marine surface ships. Si *et al.* [51] found that the ADRC approach can control pollutant release in a long-distance tunnel via longitudinal ventilation. To address the precise locating control problem of a polar crane with center of gravity shifting, cross-coupling, and external disturbance, the ADRC system was utilized in the paper [52].

In this study, two ADRCs with identical structures were designed for the two decoupled linear subsystems. The unmodeled dynamics of the motor, the variation of motor parameters due to heating, and the unknown disturbances

of the motor system were estimated by an extended state observer (ESO) in the ADRC. When comparing with the classical PID control method, the control system of this study exhibited stronger robustness for the variations of the motor parameters and load torque. As such, the essence of the theory and method for the affine nonlinear system's feedback linearization and precise decoupling and ADRC are fully absorbed. First, the nonlinear feedback linearization method was used to transform the complex, nonlinear, and coupled nominal motor dynamics model into two simple, linear, and decoupled subsystems: rotor speed and flux linkage. Second, two ADRC controllers with identical structures were designed for the two subsystems, which allows the motor to start quickly and shortens the transition process of the electromagnetic torque when the motor is suddenly loaded. Finally, the energy consumption during the starting and transition processes for the control system was examined with the power saving rate compared against the open-loop system.

There are eight parts in this paper. Part I serves as the literature review. In part II, we described a condition where a multi-input multi-output (MIMO) affine nonlinear system could be linearized. In part III, we established the dynamic equation of the hoisting motor drag system for the lifting mechanism of the crane. Part IV details the mathematical model of the motor. Based on the theory and method of the part II, we obtained the AC induction motor's two completely decoupled second-order linear subsystems (rotor speed and flux linkage) in the part V. In part VI, two ADRCs with identical structures were designed for the rotor speed and flux linkage subsystems. In parts VII and VIII, important conclusions were drawn through experimental study.

## II. RELATIVE ORDER VECTOR AND RELATIVE ORDER OF AFFINE NONLINEAR SYSTEM

Consider a multi-input multi-output (MIMO) affine nonlinear system,

$$\begin{cases} \dot{\mathbf{x}} = \mathbf{f}(\mathbf{x}) + \mathbf{g}(\mathbf{x})\mathbf{u} \\ \mathbf{y} = \mathbf{h}(\mathbf{x}), \end{cases} \quad (1)$$

where  $\mathbf{x} \in \mathbb{R}^n$ ,  $\mathbf{u} \in \mathbb{R}^m$ , and  $\mathbf{y} \in \mathbb{R}^m$  are the  $n$ -dimensional state variables and the  $m$ -dimensional input and output vectors, respectively. Moreover,  $\mathbf{x} = [x_1 \ x_2 \ \cdots \ x_n]^T$ ,  $\mathbf{u} = [u_1 \ u_2 \ \cdots \ u_m]^T$ , and  $\mathbf{y} = [y_1 \ y_2 \ \cdots \ y_m]^T$ . The functions  $\mathbf{f}(\mathbf{x}) = [f_1(\mathbf{x})f_2(\mathbf{x}) \cdots f_n(\mathbf{x})]^T$  and  $\mathbf{g}(\mathbf{x}) = [g_1(\mathbf{x}) \ g_2(\mathbf{x}) \ \cdots \ g_m(\mathbf{x})]^T$  are  $n$ -dimensional and  $m$ -dimensional sufficiently smooth vector fields, respectively, where  $f_i(\mathbf{x})(i = 1, 2, \cdots, n)$  is scalar function and  $g_j(\mathbf{x})(j = 1, 2, \cdots, m)$  is an  $n$ -dimensional column vector. The function  $\mathbf{h}(\mathbf{x}) = [h_1(\mathbf{x}) \ h_2(\mathbf{x}) \ \cdots \ h_m(\mathbf{x})]^T$ , where  $h_j(\mathbf{x})(j = 1, 2, \cdots, m)$  is a smooth scalar function.

Each output in the MIMO system given by Eq. (1),  $y_j = h_j(\mathbf{x})(j = 1, 2, \cdots, m)$ , has a corresponding relative order  $\gamma_j$ . When  $\mathbf{x}$  is approximately the neighborhood of  $\mathbf{x}(\mathbf{0})$ , if the following conditions are true,  $\boldsymbol{\gamma} = (\gamma_1 \ \gamma_2 \ \cdots \ \gamma_m)$  is called the relative order vector of Equation (1). The relative order

number is  $\gamma_j(j = 1, 2, \dots, m)$ , e.g.,  $k_i < \gamma_i - 1$ ,

$$L_{g_j} L_f^{k_i} h_j(x) = 0 \quad (j = 1, 2, \dots, m), \quad (2)$$

where  $L_f^{k_i} h_j(x)$  is the  $r$ -th order Lie derivative of the  $j$ -th output function  $h_j(x)$  with respect to the vector field  $f(x)$ ,  $L_{g_j} L_f^{k_i} h_j(x)$  is the Lie derivative of  $L_f^{k_i} h_j(x)$  with respect to the  $j$ -th column  $n$ -dimensional column vector  $g_j(x)$ .

The following matrix is defined:

$$D(x) = \begin{bmatrix} L_{g_1} L_f^{\gamma_1-1} h_1(x) & L_{g_2} L_f^{\gamma_1-1} h_1(x) & \dots & L_{g_m} L_f^{\gamma_1-1} h_1(x) \\ L_{g_1} L_f^{\gamma_2-1} h_2(x) & L_{g_2} L_f^{\gamma_2-1} h_2(x) & \dots & L_{g_m} L_f^{\gamma_2-1} h_2(x) \\ \vdots & \vdots & \vdots & \vdots \\ L_{g_1} L_f^{\gamma_m-1} h_m(x) & L_{g_2} L_f^{\gamma_m-1} h_m(x) & \dots & L_{g_m} L_f^{\gamma_m-1} h_m(x) \end{bmatrix} \quad (3)$$

where  $L_f^{\gamma_m-1} h_m(x)$  is the  $(\gamma_m - 1)$ -th order Lie derivative of the scalar function  $h_m(x)$  with respect to the vector field  $f(x)$ , i.e., the rate of change of  $h_m(x)$  in the  $f(x)$  direction.

### III. EQUIVALENT LOAD TORQUE AND SYSTEM DYNAMIC EQUATION OF CRANE'S HOIST MOTOR DRAG SYSTEM

The hoisting motor drive system's lifting mechanism of the crane is shown in Fig. 1(a). The motor output electromagnetic torque is  $T_e$ . The motor rotor speed  $n$  is transferred to the hoisting drum through the intermediate decelerating mechanism, and then the load ( $m_L + m_0$ , where  $m_0$  is the mass of spreader) is lifted through the pulley block with speed  $v_L$ . The rotation radius and mass of the pulley block are not considered. When the lifting load falls, the motor operates in a state of power generation, and then the motor no longer consumes the electric energy from the power grid. In practice, energy-consumption or mechanical-brake braking is generally used to consume electric energy generated by the motor, so electric energy consumption by the motor is only considered when the lifting load rises.

To facilitate the calculation, the single-shaft motor drive system shown in Fig. 1 (b) is equivalent to the multi-shaft motor drive system shown in Fig. 1 (a), and the positive direction of each physical quantity is specified in Fig. 1 (c). Based on the principle that the kinetic energy of the transmission system is invariable, the equivalent moment of inertia of the motor's rotor shaft is obtained as follows:

$$J = J_e + J_1 \frac{1}{j_1^2} + J_2 \frac{1}{j_2^2} + J_r \frac{1}{j_r^2} + m \left( \frac{v_L}{n} \right)^2 + \frac{W_{fd}}{n^2}, \quad (4)$$

where  $J_e$  is the moment of inertia of the motor rotor;  $J_1, J_2$ , and  $J_r$  are the moments of inertia of intermediate shaft 1, intermediate shaft 2, and the lifting drum, respectively;  $j_1 = \frac{n}{n_1}, j_2 = \frac{n}{n_2}$ , and  $j_r = \frac{n}{n_r}$  are the reduction ratios of the inertia of intermediate shaft 1, intermediate shaft 2, and the lifting drum;  $n$  is the motor's rotor speed;  $n_1, n_2$ , and  $n_r$  are the rotational speeds of intermediate shaft 1, intermediate shaft 2, and the lifting drum, respectively;  $m = \left( \frac{30}{\pi} \right)^2 (m_0 + m_L)$  is an

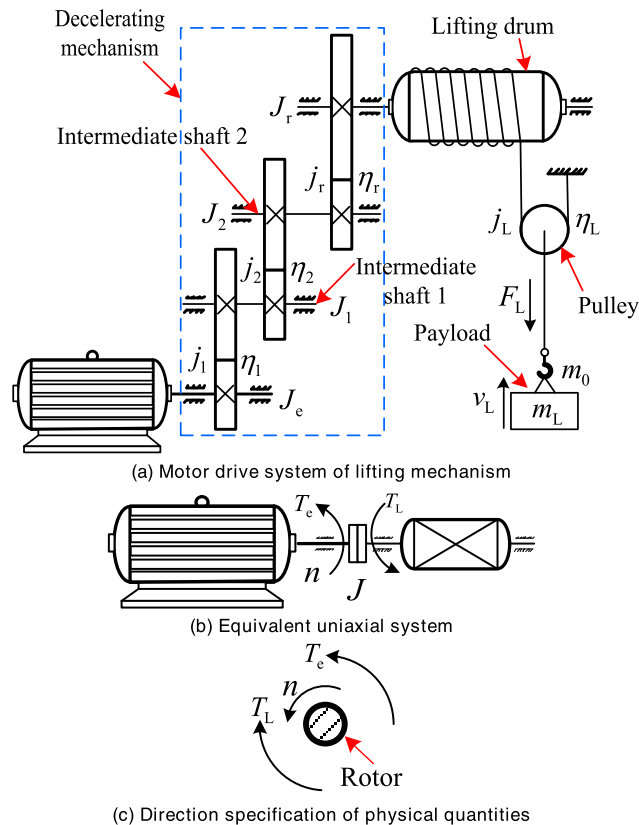


FIGURE 1. Equivalent single-shaft motor drive system of the crane.

equivalent mass;  $W_{fd} = 2 \times \left( \frac{30}{\pi} \right)^2 W_f$  is an equivalent loss; and  $W_f$  is the loss caused by friction and other factors.

In general,  $j_1^2 \gg 1, j_2^2 \gg 1, j_r^2 \gg 1$ , and  $\frac{1}{n^2} \approx 0$ . According to Eq. (4), the equivalent rotational inertia  $J$  of the transmission mechanism can only depend on the rotational inertia  $J_e$  of the motor rotor, so  $J \approx J_e$ .

The equivalent load torque on the motor rotor shaft is referred to as the load torque,

$$T_L = \frac{DF_L}{2j_1 j_2 j_r j_L \eta_1 \eta_2 \eta_r \eta_L}, \quad (5)$$

where  $D$  is the lifting drum's diameter,  $j_L = \frac{n}{n_L}$  is the pulley's deceleration ratio,  $F_L = (m_0 + m_L)g$  is the wire rope's static tension,  $g$  is the gravitational acceleration, and  $\eta_1, \eta_2, \eta_r$ , and  $\eta_L$  are the transmission efficiencies of intermediate shaft 1, intermediate shaft 2, the lifting drum, and the pulley, respectively.

According to Eq. (5), when the structure of the transmission system is known,  $T_L$  is only related to  $F_L$  and has no relation to the motor rotor speed, which is the constant torque load characteristic of the crane. The analysis shows that the equivalent conversion method of the horizontal motion mechanism of the crane's cart and trolley is the same as that expressed by Eqs. (4) and (5).

According to Fig. 1 (b), the dynamic equation of the motor drag system can be obtained as follows:

$$J \frac{d\omega_r}{dt} = T_e - T_L, \quad (6)$$

where  $\omega_r = \frac{\pi}{30}n$  is the mechanical angular velocity of the motor rotor, which is also known as the rotor mechanical angular frequency or rotor angular velocity. The electric angular velocity of the rotor is  $\omega = n_p\omega_r$ , and  $n_p$  is the motor's pole logarithm.

According to Eq. (6), when the motor's electromagnetic torque  $T_e$  is equal to the load torque  $T_L$ , the crane's lifting mechanism can operate smoothly. However, the load torque is often uncertain, which requires the electromagnetic torque  $T_e$  to quickly track the load torque  $T_L$ . The process of the electromagnetic torque  $T_e$  stabilizing at the load torque  $T_L$  is defined as the electromagnetic torque transition process of the motor, denoted as  $[t_1, t_1 + t_s]$ . In the electromagnetic torque transition process of the motor,  $t_1$  is the moment of sudden load on the motor, and  $t_s$  is the time required for the transition process. The time is known as the motor electromagnetic torque stabilization time and will henceforth be referred to as the stabilization time. The motor's starting moment is  $t_1 = 0$ , with the corresponding  $t_s$  as the starting time. When  $t_s$  is smaller, the motor's stabilizing process is shorter, and the motor has a good load tracking ability. Therefore, the key for the lifting motor's control is to control the motor's electromagnetic torque  $T_e$ , so the electromagnetic torque  $T_e$  can be stabilized at the load torque  $T_L$  in a short time. Simply the tracking and adjusting time of  $T_e$  to  $T_L$  can be shortened and the stabilization time  $t_s$  can be reduced.

#### IV. MATHEMATICAL MODEL FOR THE THREE-PHASE AC INDUCTION MOTORS

The stator windings and rotor windings of the three-phase induction motor can be transformed into the static two-phase coordinate system  $\alpha$ - $\beta$  as shown in Fig. 2 by coordinate and rotation transformation. In Fig. 2,  $u_{s\alpha}$  and  $u_{s\beta}$  are stator voltages, whereas  $u_{r\alpha}$  and  $u_{r\beta}$  are rotor voltages. Considering that the cage rotor is short circuit, generally  $u_{r\alpha} = u_{r\beta} = 0$ . In addition,  $i_{s\alpha}$  and  $i_{s\beta}$  are the stator currents, whereas  $i_{r\alpha}$  and  $i_{r\beta}$  are the rotor currents. From Fig. 2, the voltage equation of the motor can be written as

$$\begin{bmatrix} u_{s\alpha} \\ u_{s\beta} \\ 0 \\ 0 \end{bmatrix} = \begin{bmatrix} R_s & 0 & 0 & 0 \\ 0 & R_s & 0 & 0 \\ 0 & 0 & R_r & 0 \\ 0 & 0 & 0 & R_r \end{bmatrix} \begin{bmatrix} i_{s\alpha} \\ i_{s\beta} \\ i_{r\alpha} \\ i_{r\beta} \end{bmatrix} + \frac{d}{dt} \begin{bmatrix} \psi_{s\alpha} \\ \psi_{s\beta} \\ \psi_{r\alpha} \\ \psi_{r\beta} \end{bmatrix} + \begin{bmatrix} 0 \\ 0 \\ \omega_r \psi_{r\beta} \\ -\omega_r \psi_{r\alpha} \end{bmatrix}, \quad (7)$$

where  $R_s$  and  $R_r$  are the stator and rotor resistances,  $\psi_{s\alpha}$  and  $\psi_{s\beta}$  are stator flux linkages,  $\psi_{r\alpha}$  and  $\psi_{r\beta}$  are rotor flux linkages.

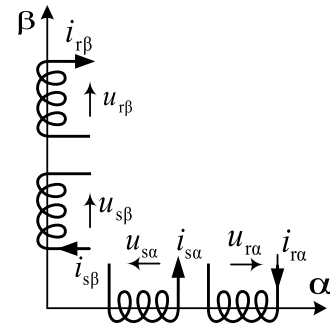


FIGURE 2. Static two-phase coordinate system  $\alpha$ - $\beta$  of the motor.

The flux equation of the motor can be written as

$$\begin{bmatrix} \psi_{s\alpha} \\ \psi_{s\beta} \\ \psi_{r\alpha} \\ \psi_{r\beta} \end{bmatrix} = \begin{bmatrix} L_s & 0 & L_m & 0 \\ 0 & L_s & 0 & L_m \\ L_m & 0 & L_r & 0 \\ 0 & L_m & 0 & L_r \end{bmatrix} \begin{bmatrix} i_{s\alpha} \\ i_{s\beta} \\ i_{r\alpha} \\ i_{r\beta} \end{bmatrix}, \quad (8)$$

where  $L_s$  and  $L_r$  are the stator and rotor inductances, and  $L_m$  is the mutual inductance between the stator and rotor.

The torque equation of the motor is

$$T_e = n_p L_m (i_{s\beta} i_{r\alpha} - i_{s\alpha} i_{r\beta}). \quad (9)$$

The variables  $\omega_r$ ,  $\psi_{r\alpha}$ ,  $\psi_{r\beta}$ ,  $i_{s\alpha}$ , and  $i_{s\beta}$  are selected as the state variables. According to Eqs. (6)–(9), the mathematical model of the motor can be written as

$$\begin{cases} \frac{d\omega_r}{dt} = k(\psi_{r\alpha} i_{s\beta} - \psi_{r\beta} i_{s\alpha}) - \frac{T_L}{J} \\ \frac{d\psi_{r\alpha}}{dt} = -\vartheta \psi_{r\alpha} - n_p \omega_r \psi_{r\beta} + \vartheta L_m i_{s\alpha} \\ \frac{d\psi_{r\beta}}{dt} = n_p \omega_r \psi_{r\alpha} - \vartheta \psi_{r\beta} + \vartheta L_m i_{s\beta} + \frac{u_{s\alpha}}{\delta} \\ \frac{di_{s\alpha}}{dt} = \vartheta \varepsilon \psi_{r\alpha} + n_p \varepsilon \omega_r \psi_{r\beta} - \xi i_{s\alpha} + \frac{u_{s\beta}}{\delta} \\ \frac{di_{s\beta}}{dt} = -n_p \varepsilon \omega_r \psi_{r\alpha} + \vartheta \varepsilon \psi_{r\beta} - \xi i_{s\beta}, \end{cases} \quad (10)$$

where  $\delta = L_s - \frac{L_m^2}{L_r}$ ,  $\vartheta = \frac{R_r}{L_r}$ ,  $\varepsilon = \frac{L_m}{\delta L_r}$ ,  $\xi = \frac{L_m^2 R_r}{\delta L_r^2} + \frac{R_s}{\delta}$ , and  $k = 1.5 \frac{n_p L_m}{J L_r}$ .

#### V. PRECISE LINEARIZATION AND DECOUPLING OF DYNAMIC MODEL OF LIFTING MOTOR

The dynamic model (Eq.(10)) in the static two-phase coordinate system  $\alpha$ - $\beta$  can be described using Eq. (1), where the state variable vector is  $\mathbf{x} = [\omega_r \ \psi_{r\alpha} \ \psi_{r\beta} \ i_{s\alpha} \ i_{s\beta}]^T$ ,  $h(\mathbf{x}) = [\omega_r, \ \psi_{r\alpha}^2 + \psi_{r\beta}^2]^T$ , the output  $y_1 = \omega_r$  is the angular velocity of the rotor, and  $y_2 = \psi_{r\alpha}^2 + \psi_{r\beta}^2$  is the sum of squares of the amplitude of the rotor flux, which is also referred to as the



rotor flux. The following functions are defined as

$$f(x) = \begin{bmatrix} k(\psi_{r\alpha} i_{s\beta} - \psi_{r\beta} i_{s\alpha}) - \frac{T_L}{J} \\ -\vartheta \psi_{r\alpha} - n_p \omega_r \psi_{r\beta} + \vartheta L_m i_{s\alpha} \\ n_p \omega_r \psi_{r\alpha} - \vartheta \psi_{r\beta} + \vartheta L_m i_{s\beta} \\ \vartheta \varepsilon \psi_{r\alpha} + n_p \varepsilon \omega_r \psi_{r\beta} - \xi i_{s\alpha} \\ -n_p \varepsilon \omega_r \psi_{r\alpha} + \vartheta \varepsilon \psi_{r\beta} - \xi i_{s\beta} \end{bmatrix},$$

$$g(x) = [g_1 \quad g_2] = \begin{bmatrix} 0 & 0 \\ 0 & 0 \\ 0 & 0 \\ \delta^{-1} & 0 \\ 0 & \delta^{-1} \end{bmatrix}, \quad u = \begin{bmatrix} u_{s\alpha} \\ u_{s\beta} \end{bmatrix}.$$

According to Eq. (2), the relative order vector of the AC induction motor is  $\gamma = (\gamma_1, \gamma_2)$ , where  $\gamma_1 = \gamma_2 = 2$ , and

$$D(x) = \begin{bmatrix} L_{g_1} L_f h_1(x) & L_{g_2} L_f h_1(x) \\ L_{g_1} L_f h_2(x) & L_{g_2} L_f h_2(x) \end{bmatrix}, \quad (11)$$

where  $L_{g_1} L_f h_1(x) = -\frac{k}{\delta} \psi_{r\beta}$ ,  $L_{g_2} L_f h_1(x) = \frac{k}{\delta} \psi_{r\alpha}$ ,  $L_{g_1} L_f h_2(x) = \frac{2\vartheta L_m}{\delta} \psi_{r\alpha}$ ,  $L_{g_2} L_f h_2(x) = \frac{2\vartheta L_m}{\delta} \psi_{r\beta}$ ,  $L_f h_1(x) = k(\psi_{r\alpha} i_{s\beta} - \psi_{r\beta} i_{s\alpha}) - \frac{T_L}{J}$ , and  $L_f h_2(x) = -2\vartheta(\psi_{r\alpha}^2 + \psi_{r\beta}^2) + 2\vartheta L_m(\psi_{r\alpha} i_{s\alpha} + \psi_{r\beta} i_{s\beta})$ .

Because  $\text{Det}(D(x)) = -2\frac{\vartheta L_m k}{\delta^2}(\psi_{r\alpha}^2 + \psi_{r\beta}^2) \neq 0$ ,  $D(x)$  is a nonsingular matrix, and  $D(x)$ 's inverse matrix is

$$D^{-1}(x) = \frac{\delta}{\psi_{r\alpha}^2 + \psi_{r\beta}^2} \begin{bmatrix} -\frac{\psi_{r\beta}}{k} & \frac{\psi_{r\alpha}}{2\vartheta L_m} \\ \frac{\psi_{r\alpha}}{k} & \frac{\psi_{r\beta}}{2\vartheta L_m} \end{bmatrix}. \quad (12)$$

The following coordinate transformation is defined as

$$\begin{cases} z_1 = h_1(x) \\ z_2 = L_f h_1(x) \\ z_3 = h_2(x) \\ z_4 = L_f h_2(x) \\ z_5 = \arctan\left(\frac{\psi_{r\beta}}{\psi_{r\alpha}}\right), \end{cases} \quad (13)$$

where  $z_3 = y_2 = h(x) = \psi_{r\alpha}^2 + \psi_{r\beta}^2$  is the sum of squares of the amplitude of the rotor flux. In general,  $z_3$  is not equal to zero if the motor is energized, and a magnetic field can be built into the motor. So, the inverse transformation is

$$\begin{cases} \omega_r = z_1 \\ \psi_{r\alpha} = \sqrt{z_3} \cos z_5 \\ \psi_{r\beta} = \sqrt{z_3} \sin z_5 \\ i_{s\alpha} = \frac{1}{\sqrt{z_3}} \left[ \cos(z_5(\frac{z_4 + 2\vartheta z_3}{2\vartheta L_m})) - \frac{1}{k} \sin(z_5(z_2 + \frac{T_L}{J})) \right] \\ i_{s\beta} = \frac{1}{\sqrt{z_3}} \left[ \sin(z_5(\frac{z_4 + 2\vartheta z_3}{2\vartheta L_m})) + \frac{1}{k} \cos(z_5(z_2 + \frac{T_L}{J})) \right] \end{cases} \quad (14)$$

Therefore, in the new coordinate, the AC induction motor's dynamic model is

$$\begin{cases} \dot{z}_1 = z_2 \\ \dot{z}_2 = L_f^2 h_1(x) + L_{g_1} L_f h_1(x) u_{s\alpha} + L_{g_2} L_f h_1(x) u_{s\beta} \\ \dot{z}_3 = z_4 \\ \dot{z}_4 = L_f^2 h_2(x) + L_{g_1} L_f h_2(x) u_{s\alpha} + L_{g_2} L_f h_2(x) u_{s\beta} \\ \dot{z}_5 = z_1 + \frac{\vartheta L_m}{k z_3} (z_2 + \frac{n_p}{J} T_L) \\ y_1 = z_1 \\ y_2 = z_3, \end{cases} \quad (15)$$

where

$$L_f^2 h_1(x) = -k \varepsilon n_p \omega_r (\psi_{r\alpha}^2 + \psi_{r\beta}^2) - k(\vartheta + \xi) \times (\psi_{r\alpha} i_{s\beta} - \psi_{r\beta} i_{s\alpha}) - k n_p \omega_r (\psi_{r\alpha} i_{s\alpha} - \psi_{r\beta} i_{s\beta}),$$

and

$$L_f^2 h_2(x) = (4\vartheta^2 + 2\vartheta^2 \varepsilon L_m)(\psi_{r\alpha}^2 + \psi_{r\beta}^2) + 2\vartheta L_m n_p \omega_r (\psi_{r\alpha} i_{s\beta} - \psi_{r\beta} i_{s\alpha}) - (6\vartheta^2 L_m + 2\vartheta \xi L_m)(\psi_{r\alpha} i_{s\alpha} + \psi_{r\beta} i_{s\beta}) + 2\vartheta^2 L_m^2 (i_{s\alpha}^2 + i_{s\beta}^2).$$

The first four equations can be written based on Eq. (11) as follows:

$$\begin{bmatrix} \ddot{y}_1 \\ \ddot{y}_2 \end{bmatrix} = \begin{bmatrix} L_f^2 h_1(x) \\ L_f^2 h_2(x) \end{bmatrix} + D(x) \begin{bmatrix} u_{s\alpha} \\ u_{s\beta} \end{bmatrix}. \quad (16)$$

The virtual control inputs are defined as  $v_1$  and  $v_2$ , and

$$\begin{bmatrix} v_1 \\ v_2 \end{bmatrix} = \begin{bmatrix} L_f^2 h_1(x) \\ L_f^2 h_2(x) \end{bmatrix} + D(x) \begin{bmatrix} u_{s\alpha} \\ u_{s\beta} \end{bmatrix}. \quad (17)$$

The actual control input of the motor is

$$\begin{bmatrix} u_{s\alpha} \\ u_{s\beta} \end{bmatrix} = D^{-1}(x) \left( \begin{bmatrix} v_1 \\ v_2 \end{bmatrix} - \begin{bmatrix} L_f^2 h_1(x) \\ L_f^2 h_2(x) \end{bmatrix} \right). \quad (18)$$

Based on Eqs. (16)–(18), we obtain the AC induction motor's two completely decoupled second-order linear subsystems, rotor speed subsystem I and flux linkage subsystem II, as follows:

$$\text{I: } \begin{cases} \dot{z}_1 = z_2 \\ \dot{z}_2 = v_1 \\ y_1 = z_1, \end{cases} \quad (19\text{-a})$$

$$\text{II: } \begin{cases} \dot{z}_3 = z_4 \\ \dot{z}_4 = v_2 \\ y_2 = z_3. \end{cases} \quad (19\text{-b})$$

The virtual control inputs,  $v_1$  and  $v_2$ , can independently control the motor rotor speed  $y_1 = \omega_r$ , and the sum of squares of the rotor flux amplitude,  $y_2 = \psi_{r\alpha}^2 + \psi_{r\beta}^2$ , which greatly reduces the design difficulty of the controller. Moreover, the matrix  $\begin{bmatrix} L_f^2 h_1(x) \\ L_f^2 h_2(x) \end{bmatrix}$  is called the decoupling device, and the matrix  $D^{-1}(x)$  serves as the inverter.

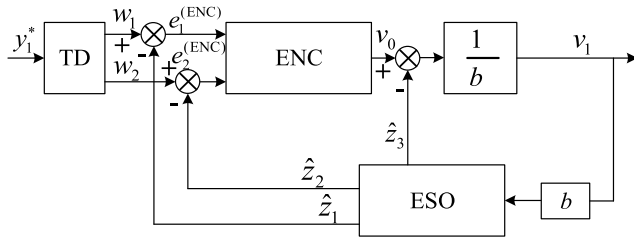


FIGURE 3. Block diagram of speed ADRC's structure.

## VI. DESIGN OF THE ADRC FOR THE CRANE MOTOR DECOUPLING SYSTEM

The stator or rotor resistance varies in the vicinity of the rated value because of the motor temperature rise, and the uncertainty of the load torque magnitude. Thus, the goal of the AC induction motor control was to control the stator voltages  $u_{s\alpha}$  and  $u_{s\beta}$ . When the rotor speed  $\omega_r$  and the sum of squares of the amplitude of the rotor flux  $y_2 = \psi_{r\alpha}^2 + \psi_{r\beta}^2$  are given by reference values, the motor's electromagnetic torque  $T_e$  can quickly track the unknown load torque  $T_L$ . Therefore, with regard to the second-order linear subsystems I and II, we designed two controllers with the same structure: motor speed ADRC and flux ADRC. The motor speed ADRC included a tracking differentiation (TD), error nonlinear combiner (ENC), and extended state observer (ESO), as shown in Fig. 3. The function of each part and the discrete form of the algorithm are illustrated through the speed ADRC as an example.

(1) Tracking differentiator: The transition process is arranged according to the set reference value, and the differential signal is extracted. The algorithm is as follows:

$$\begin{cases} e^{(TD)} = w_1 - y_1^* \\ w_1(k+1) = w_1(k) + Tw_2(k) \\ w_2(k+1) = w_2(k) + T \text{fhan}(e^{(TD)}, w_2, r, h), \end{cases} \quad (20)$$

where,  $w_1$  and  $w_2$  are the TD's outputs,  $e^{(TD)}$  is the tracking deviation of a variable from a given reference value,  $r$  is the speed factor that determines how fast the variable can track a given reference value,  $h$  is the filtering factor that determines the filtering effect, and  $T$  is the integral step. The function fhan of variables  $m, n, r$ , and  $h$  is denoted as

$$\text{fhan}(m, n, r, h) = -r \left( \frac{a}{d} \right) \text{fsg}(a, d) - r \text{sign}(a) \times (1 - \text{fsg}(a, d)), \quad (21)$$

where  $d = rh^2$ ,  $a_0 = hm$ ,  $p = m + a_0$ ,  $a_1 = \sqrt{d(d + 8|p|)}$ ,  $a_2 = a_0 + 0.5\text{sign}(p)(a_1 - d)$ , and  $a = (a_0 + p)\text{fsg}(p, d) + a_2(1 - \text{fsg}(p, d))$ . The function  $\text{fsg}(p, d) = 0.5(\text{sign}(p + d) - \text{sign}(p - d))$  depends on variables  $p$  and  $d$ .

(2) Extended state observer: The ESO estimates the rotor speed subsystem state variables  $z_1$  and  $z_2$  and expands the unmodeled dynamics of the motor, motor parameter changes caused by heating and other sources, and unknown disturbances of the system into new state variable  $z_3$  (hereinafter

referred to as the expanded state). The continuous-time model of ESO is as follows:

$$\begin{cases} \dot{\hat{z}}_1 = \hat{z}_2 - \beta_1^{(ESO)} e^{(ESO)} \\ \dot{\hat{z}}_2 = \hat{z}_3 - \beta_2^{(ESO)} fe + bv_1 \\ \dot{\hat{z}}_3 = -\beta_3^{(ESO)} fe_1, \end{cases} \quad (22)$$

where  $\beta^{(ESO)} = [\beta_1^{(ESO)}, \beta_2^{(ESO)}, \beta_3^{(ESO)}]$  is the parameter of ESO, and  $e^{(ESO)} = \hat{z}_1 - y_1$ .

Furthermore, Eq. (22) can estimate  $z_3$ , and the algorithm is as follows:

$$\begin{cases} e^{(ESO)} = \hat{z}_1 - y_1 \\ \hat{z}_1(k+1) = \hat{z}_1(k) + T(\hat{z}_2(k) - \beta_1^{(ESO)} e^{(ESO)}) \\ \hat{z}_2(k+1) = \hat{z}_2(k) + T(\hat{z}_3(k) - \beta_2^{(ESO)} fe + bv_1) \\ \hat{z}_3(k+1) = \hat{z}_3(k) + T(-\beta_3^{(ESO)} fe_1), \end{cases} \quad (23)$$

where  $\hat{z}_1$ ,  $\hat{z}_2$ , and  $\hat{z}_3$  are the estimated values of  $z_1$ ,  $z_2$ , and the expansion state  $z_3$ , respectively. Parameter  $b$  is the compensation factor of the control strength. The following functions are defined as  $fe = \text{fal}(e^{(ESO)}, 0.5, d)$  and  $fe_1 = \text{fal}(e^{(ESO)}, 0.25, d)$ , and  $\text{fal}$  is a function of variables  $e, a$ , and  $d$ , and defined as follows:

$$\text{fal}(e, a, d) = ed^{a-1} \text{fsg}(e, d) + |e|^a \text{sign}(e)(1 - \text{fsg}(e, d)). \quad (24)$$

(3) Error nonlinear combiner: The ENC realizes the nonlinear combination of the error feedback, and the algorithm is as follows:

$$v_0 = \beta_1^{(ENC)} \text{fal}(e_1^{(ENC)}, 0.75, d) + \beta_2^{(ENC)} \text{fal}(e_2^{(ENC)}, 1.25, d), \quad (25)$$

where  $e_1^{(ENC)} = w_1 - \hat{z}_1$  and  $e_2^{(ENC)} = w_2 - \hat{z}_2$ .

The virtual control input of the rotor speed subsystem is

$$v_1 = v_0 - \frac{\hat{z}_3}{b}. \quad (26)$$

Using the same algorithm and Eqs. (20)–(26), the AC induction motor flux linkage ADRC can also be designed, in the exact same manner as the motor speed ADRC.

The principle block diagram of the motor ADRC system based on accurate decoupling is shown in Fig. 4. As shown in Fig. 4, the decoupling device achieves precise decoupling of the motor dynamics model. The ADRC outputs are the virtual control  $v_1$  of the speed subsystem and the virtual control  $v_2$  of the flux linkage subsystem. The inverter calculates the actual control voltages of motor stator  $u_{s\alpha}$  and  $u_{s\beta}$  using Eq. (18), and  $u_{s\alpha}$  and  $u_{s\beta}$  are transformed into the PWM's three-phase modulation signals  $u_A^*$ ,  $u_B^*$ , and  $u_C^*$ , through the transformation from the two-phase coordinate  $\alpha - \beta$  to the three-phase coordinate A-B-C.

Finally, we obtain the actual three-phase control voltages of the motor  $u_A$ ,  $u_B$ , and  $u_C$ . The rotor flux  $\psi_{r\alpha}$  and  $\psi_{r\beta}$  can

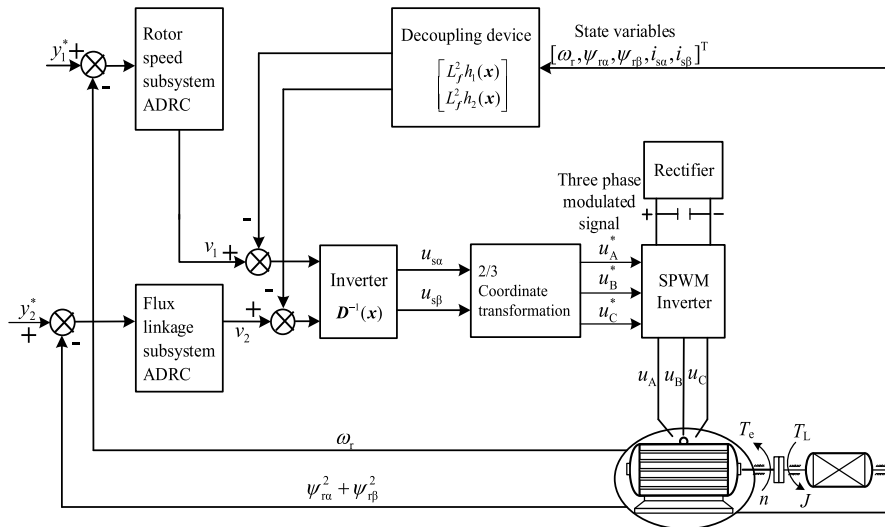


FIGURE 4. Schematic diagram of ADRC system.

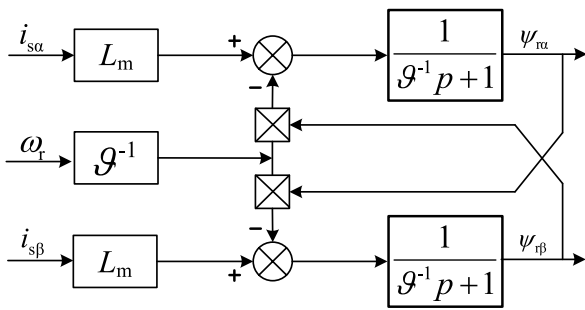


FIGURE 5. Calculation block diagram of the rotor flux linkage.

be calculated by the stator current  $i_{s\alpha}$  and  $i_{s\beta}$ , and

$$\begin{cases} \psi_{r\alpha} = \frac{1}{\vartheta^{-1}p + 1} (L_m i_{s\alpha} - \omega_r \vartheta^{-1} \psi_{r\beta}) \\ \psi_{r\beta} = \frac{1}{\vartheta^{-1}p + 1} (L_m i_{s\beta} - \omega_r \vartheta^{-1} \psi_{r\alpha}), \end{cases} \quad (27)$$

where  $p = \frac{d}{dt}$  is the differential operator.

The calculation block diagrams of  $\psi_{r\alpha}$  and  $\psi_{r\beta}$  are shown in Fig. 5. The computer flow chart is shown in Fig. 6.

## VII. EXPERIMENTAL STUDY

The experimental platform with container gantry crane is shown in Fig. 7. Different loads were provided with containers with different qualities for the hoisting motor drive system of the crane. The main controller was YASKAWA MP3300. The sampling time was 10 ms. The motor parameters were as follows:  $R_s = 0.082 \Omega$ ,  $R_r = 0.05 \Omega$ ,  $L_s = 3.44 \text{ mH}$ ,  $L_r = 3.44 \text{ mH}$ ,  $L_m = 0.027 \text{ mH}$ ,  $n_p = 2$ , and  $J = 0.37 \text{ kg}\cdot\text{m}^2$ . The nominal torque was  $T_N = 80 \text{ N}\cdot\text{m}$ . The nominal speed was  $n_N = 1480 \text{ r/min} = 155 \text{ rad/s}$ .

The ADRC parameters were as follows: for the rotor speed subsystem,  $r = 500$ ,  $h = 0.01$ ,  $T = 0.001$ ,  $\beta^{(\text{ESO})} = [800, 562, 200]$ ,  $\beta^{(\text{ENC})} = [3000, 26]$ ,  $d = 0.01$ , and  $b = 1$ .

For the flux linkage subsystem, they are  $r = 600$ ,  $\beta^{(\text{ESO})} = [2000, 2000, 2000]$ ,  $\beta^{(\text{ENC})} = [1000, 100]$ ,  $d = 0.01$ , and  $b = 1$ .

### A. VARIABLE DYNAMIC RESPONSE

To study the control effect of the closed-loop system with ADRC, we selected the motor load starting operation. Figs. 8 and 9 show the comparative results of the motor's rotational speed, flux linkage, and electromagnetic torque dynamic response of the open-loop system (no control system) and the closed-loop system when the motor was started with the rated load. The speed of the open-loop system was stable at the rated speed at about 1.3 s, and the flux was stable at  $0.94 \text{ Wb}^2$  at about 1.3 s. The closed-loop system could reach the reference speed of  $104.7 \text{ rad/s}$  at about 1.3 s without overshoot, and the flux could reach the reference flux of  $0.81 \text{ Wb}^2$  at about 0.3 s without overshoot.

The dynamic response of the electromagnetic torque is shown in Fig. 10. The electromagnetic torque of the open-loop system stabilized at the load torque when  $t_s = 1.3 \text{ s}$  in the range of  $-250$  to  $450 \text{ N}\cdot\text{m}$ . The electromagnetic torque of the closed-loop system could be stabilized at the load torque when  $t_s = 0.7 \text{ s}$  in the range of  $0$ – $250 \text{ N}\cdot\text{m}$ . The electromagnetic torque fluctuation range and adjustment time of the closed-loop system were significantly lower than those of the open-loop system, so the starting time was reduced by  $\sim 50\%$ . The histograms of the starting times are shown in Fig. 11 where the motor was started at different load rates. From Fig. 11, the open-loop system's starting time increased with increasing load rate. For the closed-loop system, the starting time was within the range of  $0.6$ – $0.8 \text{ s}$  within the rated load range, which was less than the starting time of the open-loop system.

Based on the different percentages of the motor rated torque (load rate) range, the motor's load was divided



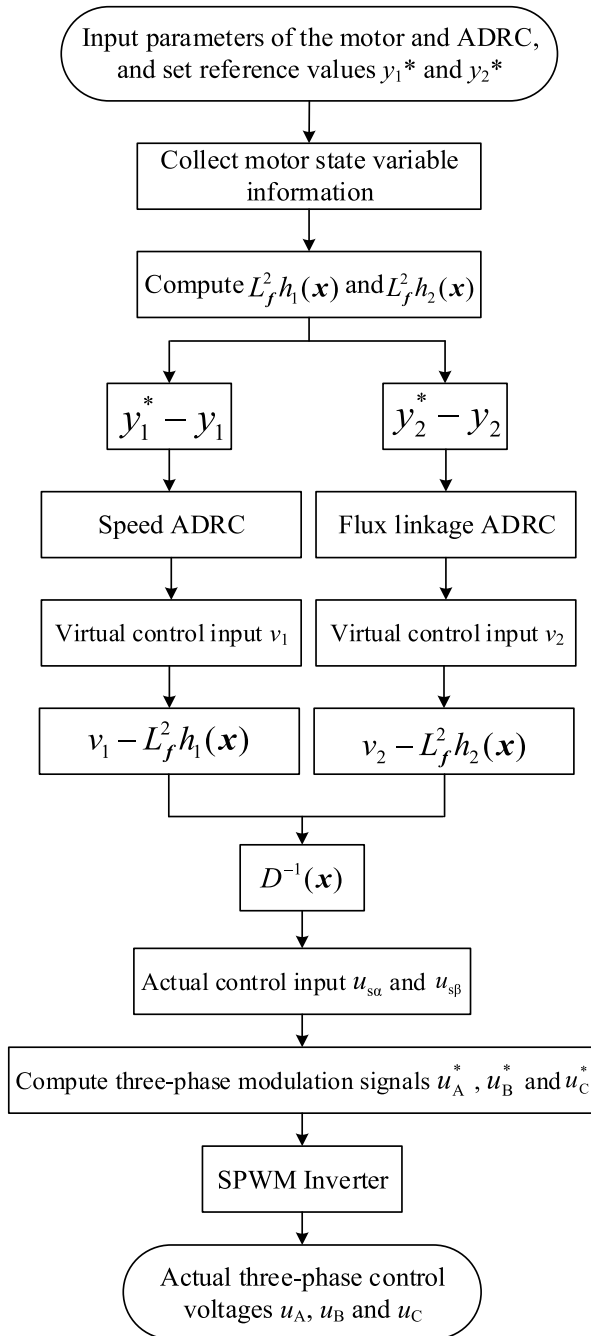


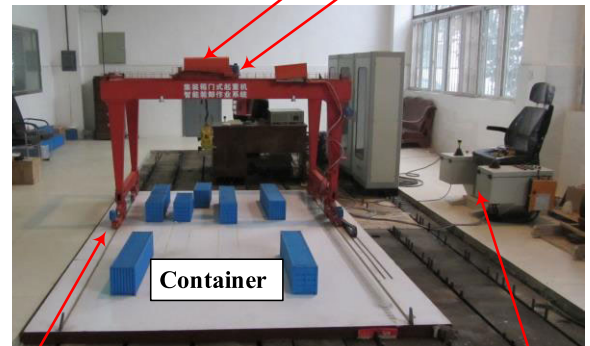
FIGURE 6. Computer flow chart.

into a light load ( $T_L \leq 30\%T_N$ ), medium-light load ( $30\%T_N < T_L < 50\%T_N$ ), medium-load ( $T_L = 50\%T_N$ ), medium-heavy load ( $50\%T_N < T_L < 80\%T_N$ ), heavy load ( $80\%T_N \leq T_L < 100\%T_N$ ), and full load ( $T_L = 100\%T_N$ ). To study the motor's transition process when the motor was suddenly loaded, the motor was initially operated under a light load ( $T_L = 24 \text{ N} \cdot \text{m}$ ) with motor subjected to a sudden load at  $t_1 = 2\text{s}$ . The rotor flux of the closed-loop system was not affected by the sudden load and was always stable at the reference flux (as shown in Fig. 12).

YASKAWA MP3300



Hoisting motor drive system Trolley motor



Cart motor

Control system



FIGURE 7. Experimental platform.

The rotor speed decreased due to the sudden load, but the rate of decrease did not exceed 7 rad/s (as shown in Fig. 13). The electromagnetic torque fluctuated when the load was suddenly applied, as shown in Fig. 14. The experiment showed that the fluctuation range of the electromagnetic torque did not exceed 20 N·m, and the fluctuation range decreased as the load rate decreased. The transition time was approximately  $t_s = 0.5 \text{ s}$ , as shown in Fig. 14, where  $E_T = T_L - T_e$  is the electromagnetic torque tracking error. Figs. 12 and 13 show that the control system achieved independent and decoupled control of the motor speed and flux linkage.

**B. ENERGY CONSUMPTION EXPERIMENT**

To analyze the ADRC closed-loop control system's energy consumption, we set motor's starting stage with different load

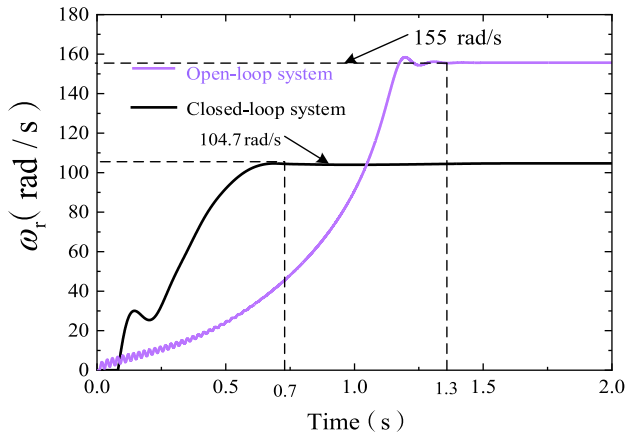


FIGURE 8. Dynamic response of the speed during the starting process at full load.

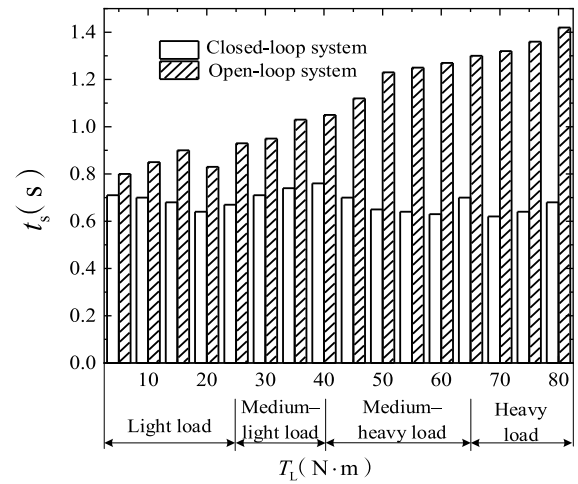


FIGURE 11. Comparison of the motor starting time.

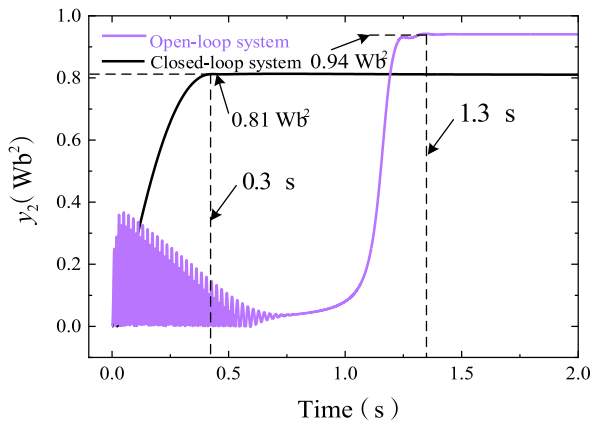


FIGURE 9. Dynamic response of the rotor flux during the starting process at full load.

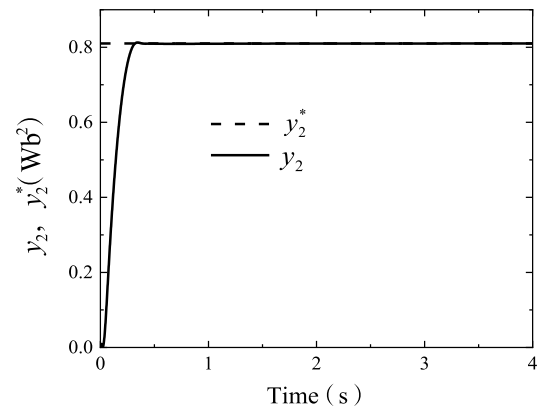


FIGURE 12. Dynamic response of the flux under abrupt load changes.

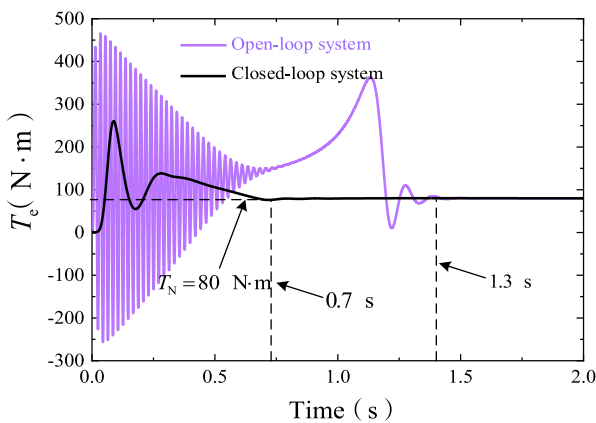


FIGURE 10. Dynamic response of the electromagnetic torque during the starting process at full load.

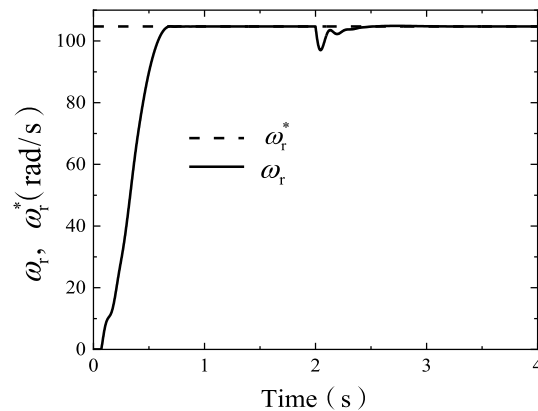


FIGURE 13. Dynamic response of the speed under abrupt load changes.

rates and the transition stage with different sudden loads. In the load's descending stage, the lifting mechanism mostly used the mechanical brake to decelerate the lifting mechanism's operation, and the motor was in a state of power generation. Thus, the energy consumption was studied only

during the lifting process. The motor's instantaneous power consumption is

$$P(t) = 3I(t)U(t), \tag{28}$$

where  $I(t)$  and  $U(t)$  are the motor's effective values of the stator current and voltage of a single phase, respectively.

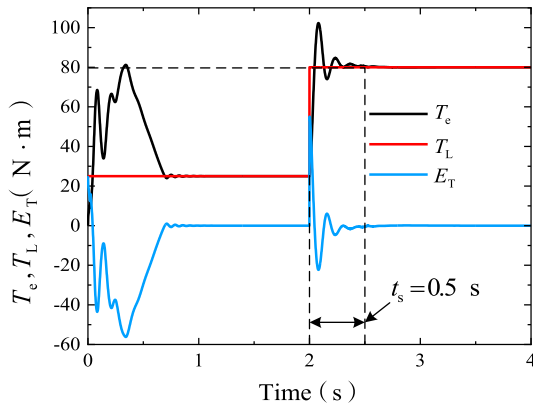


FIGURE 14. Dynamic response of the electromagnetic torque under abrupt load changes.

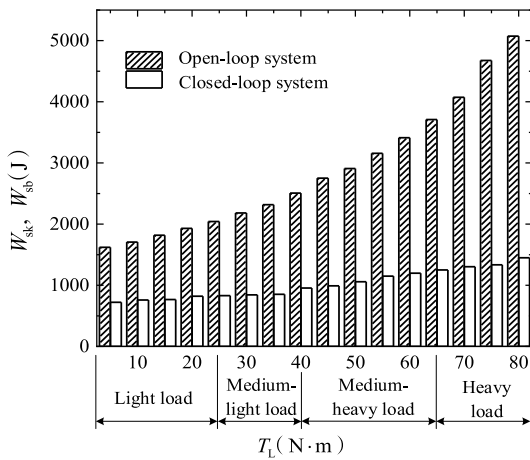


FIGURE 15. Comparison of motor starting energy consumption.

The energy consumption of the electromagnetic torque transition process  $[t_1, t_1 + t_s]$  is defined as the energy consumption of the transition process,

$$W_s = \int_{t_1}^{t_1+t_s} P(t)dt. \quad (29)$$

If  $t_1 = 0$ , the corresponding  $t_s$  is the starting time, and  $W_s$  is the starting energy consumption. According to Eq. (29), if  $P(t)$  is constant, when  $t_s$  is smaller, the motor's starting energy consumption at the same load rate is smaller, and the motor saves more energy.

The power saving rate is defined as

$$\Delta E = \frac{W_{sk} - W_{sb}}{W_{sk}} \times 100\%, \quad (30)$$

where  $W_{sk}$  and  $W_{sb}$  are the starting energy consumption ( $t_1 = 0$ ) or transition energy consumption ( $t_1 \neq 0$ ) of the open-loop system and the closed-loop system, respectively. A bar chart of the motor starting energy consumption under different loads is shown in Fig. 15. The energy consumption of the closed-loop system during the starting process was slightly larger than 1000 J under heavy load and smaller

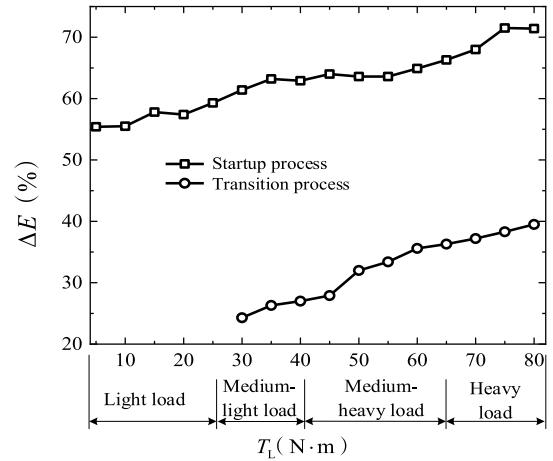


FIGURE 16. Power saving rate of the closed-loop system during the startup and transition.

than 1000 J under the other loads. For the open-loop system, the starting energy consumption was greater than that of the closed-loop system, and it increased with increasing the load rate, especially after a medium load.

The power saving rates of the closed-loop system during the starting and transition processes are shown in Fig. 16.

The closed-loop system had a significant energy saving effect during the starting process. Compared with the open-loop system, the power saving rate significantly increased as the load increased. The power saving rate was about 55%–59% under the light load and could reach 71% during the heavy load. The closed-loop system also had a significant energy saving effect in the transition process. The power saving rate was about 25% under the medium load and could reach 40% under the heavy load. This was because the closed-loop system reduced the starting time and increased the tracking speed of the electromagnetic torque to the load torque under the action of the ADRC.

During the starting process of the crane with a load, energy saving is an important factor. The ADRC closed-loop control system had a significant advantage in energy savings for the crane's starting process with a load.

### C. ROBUSTNESS EXPERIMENT

Compared with the inductance of the motor's winding, motor parameters such as the stator and rotor resistances are more likely to change because of temperature changes during operation. Furthermore, unknown disturbances in the system, reduce the accuracy of the motor dynamic model and can diminish the control performance of the control system designed for the nominal dynamics.

The ADRC system can expand the unknown model, such as the motor's unmodeled dynamics, the motor's parameter changes, and the system's unknown disturbances into a new state variable. Furthermore, it can estimate the unknown model (denoted as  $\hat{z}_3$ ) of the rotor speed subsystem and the unknown model (denoted as  $\hat{z}_1$ ) of the flux linkage subsystem,

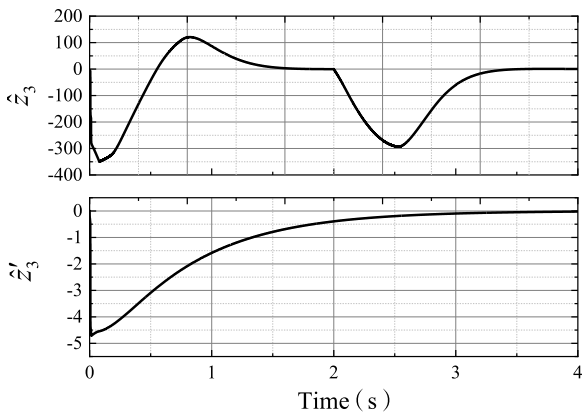


FIGURE 17. Estimation information of unknown model of motor speed and flux linkage subsystems.

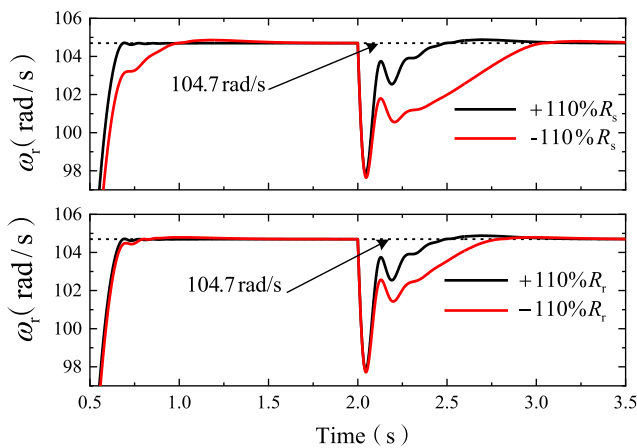


FIGURE 18. Rotor speed variations as the resistance of the stator or rotor varied.

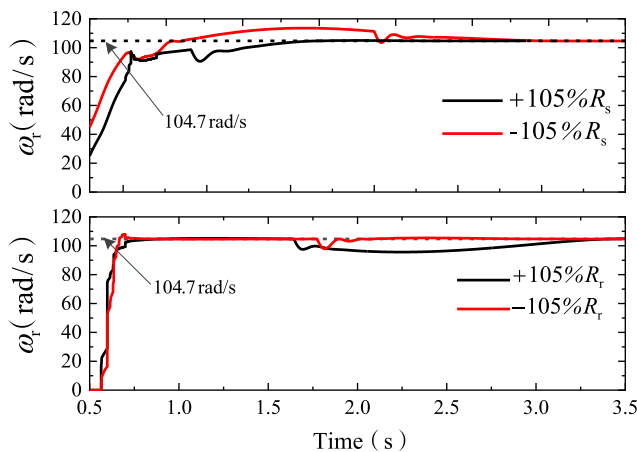


FIGURE 19. Rotor speed variations as the resistance of the stator or rotor varied.

as shown in Fig. 17. During the experiment, the load torque changed as shown in Fig. 14, and the motor stator and rotor resistances changed within  $\pm 10\%$ . The motor speed changes are shown in Fig. 18, which indicate the ADRC control

system could adapt to the motor parameter changes within a certain range. This also highlights the robustness of the control system.

ADRC is developed on the basis of a PID controller. If we used the PID control method, detailed by the paper [53] and the load torque change as shown in Fig. 14, the motor stator and rotor resistances changed less than  $\pm 5\%$ . The motor speed changes are shown in Fig. 19, which further highlight the robustness of the ADRC control system.

## VIII. CONCLUSION AND FUTRUE WORK

### A. CONCLUSION

The nonlinear feedback linearization method was used to decouple the motor's nominal dynamics model into two simple and linear subsystems: a rotor speed subsystem and a flux linkage subsystem. Two ADRC controllers with identical structures were designed for the two decoupled linear subsystems. The unmodeled dynamics of the motor, the variation of the motor parameters due to heating, and the unknown disturbances of the motor system were estimated by the ESO in the ADRC. Through a comparative experimental study of the closed-loop and the open-loop systems, the following important conclusions were drawn.

1. Compared with the open-loop system, the motor's full-load starting time was reduced by about 50%.
2. When the motor ran smoothly at different load rates and the rated load was suddenly applied, the electromagnetic torque fluctuation range did not exceed 20 N·m. The rotor flux was always stable at the reference value. The motor speed decreased, but the amount of decrease did not exceed 7 rad/s. The nominal dynamics model of the motor was completely decoupled into two independent subsystems of the rotor speed and flux linkage.
3. The starting time of the closed-loop system within the rated load range was about 0.6–0.8 s, and the starting energy consumption was less than 1000 J. The closed-loop system had a significant energy-saving effect during the motor's starting process. The power saving rate was about 55%–59% if the motor started with a light load. The power saving rate could reach 71% if the motor started with a heavy load.
4. The ADRC system could estimate the unknown model of the rotor speed and flux linkage subsystems. Furthermore, the ADRC system could adapt to the parameter variations of the motor stator and rotor resistances in the range of  $\pm 10\%$  and exhibited high robustness.

### B. FUTURE WORK

In the future, we plan to apply the theoretical research results of this paper to engineering practice. To achieve this purpose, at least three key pieces of technology need to be developed. The first is real-time monitoring or estimation of crane load torque and motor running parameters. The second is the design of hardware and programming of software for the control system. The third is the on-line setting and adjustment method of ADRC's parameters.



## ACKNOWLEDGMENT

The authors would like to thank Accdon, LLC, for its linguistic assistance during the preparation of this manuscript. They also thank the anonymous reviewers and editors for their prolific comments which significantly improved the quality of their work.

## REFERENCES

- [1] F. Chu, J. He, F. Zheng, and M. Liu, "Scheduling multiple yard cranes in two adjacent container blocks with position-dependent processing times," *Comput. Ind. Eng.*, vol. 136, pp. 355–365, Oct. 2019, doi: [10.1016/j.cie.2019.07.013](https://doi.org/10.1016/j.cie.2019.07.013).
- [2] J. He, "Berth allocation and quay crane assignment in a container terminal for the trade-off between time-saving and energy-saving," *Adv. Eng. Informat.*, vol. 30, no. 3, pp. 390–405, Aug. 2016, doi: [10.1016/j.aei.2016.04.006](https://doi.org/10.1016/j.aei.2016.04.006).
- [3] N. Sun, Y. Wu, H. Chen, and Y. Fang, "An energy-optimal solution for transportation control of cranes with double pendulum dynamics: Design and experiments," *Mech. Syst. Signal Process.*, vol. 102, pp. 87–101, Mar. 2018, doi: [10.1016/j.ymsp.2017.09.027](https://doi.org/10.1016/j.ymsp.2017.09.027).
- [4] M. M. Zheng, X. F. Zhang, S. Liang, and A. Q. Zhang, "Simulation of crane load motion trajectory based on unity 3D," in *Proc. 2nd Int. Conf. Saf. Produce Informatization (IICSPI)*, Chongqing, China, May 2019, pp. 223–226, doi: [10.1109/IICSPI48186.2019.9096031](https://doi.org/10.1109/IICSPI48186.2019.9096031).
- [5] S. Pietrosanti, F. Alasali, and W. Holderbaum, "Power management system for RTG crane using fuzzy logic controller," *Sustain. Energy Technol.*, vol. 37, pp. 1–16, Feb. 2020, doi: [10.1016/j.seta.2020.100639](https://doi.org/10.1016/j.seta.2020.100639).
- [6] G. A. Fedyayeva, T. V. Smorodova, and R. V. Kovalev, "Electromechanical system of the asynchronous electric drive of movement of a bridge crane modeling," in *Proc. 2nd Int. Conf. Ind. Eng., Appl. Manuf. (ICIEAM)*, Chelyabinsk, Russia, 2016, pp. 1–4, doi: [10.1109/ICIEAM.2016.7911593](https://doi.org/10.1109/ICIEAM.2016.7911593).
- [7] V. Papaioannou, S. Pietrosanti, W. Holderbaum, and V.-M. Becerra, "Analysis of energy usage for RTG cranes," *Energy*, vol. 125, pp. 337–344, Apr. 2017, doi: [10.1016/j.energy.2017.02.122](https://doi.org/10.1016/j.energy.2017.02.122).
- [8] Z. Bin, M. Lili, and D. Hao, "Principle of optimal voltage regulation and energy-saving for induction motor with unknown constant-torque working condition," *IEEE Access*, vol. 8, pp. 187307–187316, Oct. 2020, doi: [10.1109/ACCESS.2020.3030936](https://doi.org/10.1109/ACCESS.2020.3030936).
- [9] K. Andrzej, S. Lukasz, and M. Piotr, "Energy consumption and energy efficiency improvement of overhead crane's mechanisms," *Eksplot. Niezawodn.*, vol. 22, no. 2, pp. 323–330, 2020, doi: [10.17531/ein.2020.2.15](https://doi.org/10.17531/ein.2020.2.15).
- [10] Y. L. Chen, J. L. J. L. He, and K. Wu, "Investigation of the energy regeneration and control strategy of a crane hoisting system," *Stroj. Vestn.-J. Mech. Eng.*, vol. 64, no. 3, pp. 157–168, 2018, doi: [10.5545/sv-jme.2017.4717](https://doi.org/10.5545/sv-jme.2017.4717).
- [11] H. Taghaddos, U. Hermann, and A. Abbasi, "Automated crane planning and optimization for modular construction," *Automat. Constr.*, vol. 95, pp. 219–232, Nov. 2018, doi: [10.1016/j.autcon.2018.07.009](https://doi.org/10.1016/j.autcon.2018.07.009).
- [12] L. Scalerà, P. Gallina, S. Seriani, and A. Gasparetto, "Cable-based robotic crane (CBRC): Design and implementation of overhead traveling cranes based on variable radius drums," *IEEE Trans. Robot.*, vol. 34, no. 2, pp. 474–485, Apr. 2018, doi: [10.1109/TRO.2018.2791593](https://doi.org/10.1109/TRO.2018.2791593).
- [13] F. Alasali, S. Haben, and W. Holderbaum, "Energy management systems for a network of electrified cranes with energy storage," *Int. J. Electr. Power Energy Syst.*, vol. 106, pp. 210–222, Mar. 2019, doi: [10.1016/j.ijepes.2018.10.001](https://doi.org/10.1016/j.ijepes.2018.10.001).
- [14] B. Capelo, M. Pérez-Sánchez, J. F. P. Fernandes, H. M. Ramos, P. A. López-Jiménez, and P. J. C. Branco, "Electrical behaviour of the pump working as turbine in off grid operation," *Appl. Energy*, vol. 208, pp. 302–311, Dec. 2017, doi: [10.1016/j.apenergy.2017.10.039](https://doi.org/10.1016/j.apenergy.2017.10.039).
- [15] B. Liu, S. Wang, B. Zhao, J. Fang, and X. Wang, "Analysis and calculation of LR circuit mathematical model for high temperature superconducting induction motor," *Phys. C, Supercond. Appl.*, vol. 568, Jan. 2020, Art. no. 1353579, doi: [10.1016/j.physc.2019.1353579](https://doi.org/10.1016/j.physc.2019.1353579).
- [16] A. Trianni, E. Cagno, and D. Accordini, "Energy efficiency measures in electric motors systems: A novel classification highlighting specific implications in their adoption," *Appl. Energy*, vol. 252, Oct. 2019, Art. no. 113481, doi: [10.1016/j.apenergy.2019.113481](https://doi.org/10.1016/j.apenergy.2019.113481).
- [17] M. B. Payán, J. M. R. Fernandez, J. M. M. Ortega, and J. M. R. Santos, "Techno-economic optimal power rating of induction motors," *Appl. Energy*, vol. 240, pp. 1031–1048, Apr. 2019, doi: [10.1016/j.apenergy.2019.02.016](https://doi.org/10.1016/j.apenergy.2019.02.016).
- [18] T. A. Srinivas, G. Themozhi, and S. Nagarajan, "Current mode controlled fuzzy logic based interleaved CUK converter SVM inverter fed induction motor drive system," *Microprocess. Microsyst.*, vol. 74, Apr. 2020, Art. no. 103002, doi: [10.1016/j.micpro.2020.103002](https://doi.org/10.1016/j.micpro.2020.103002).
- [19] N. Pimkumwong and M.-S. Wang, "Full-order observer for direct Torque control of induction motor based on constant V/F control technique," *ISA Trans.*, vol. 73, pp. 189–200, Feb. 2018, doi: [10.1016/j.isatra.2017.12.014](https://doi.org/10.1016/j.isatra.2017.12.014).
- [20] I. Karatzafaris, E. C. Tatakis, and N. Papanikolaou, "Investigation of energy savings on industrial motor drives using bidirectional converters," *IEEE Access*, vol. 5, pp. 17952–17961, Sep. 2017, doi: [10.1109/ACCESS.2017.2748621](https://doi.org/10.1109/ACCESS.2017.2748621).
- [21] M. J. S. Zuberi, A. Tjrdink, and M. K. Patel, "Techno-economic analysis of energy efficiency improvement in electric motor driven systems in Swiss industry," *Appl. Energy*, vol. 205, pp. 85–104, Nov. 2017, doi: [10.1016/j.apenergy.2017.07.121](https://doi.org/10.1016/j.apenergy.2017.07.121).
- [22] A. Naveed, A. Ghulam, and A. Rabeh, "Power quality analysis of the output voltage of AC voltage and frequency controllers realized with various voltage control techniques," *Appl. Sci.*, vol. 11, no. 2, pp. 1–24, Jan. 2021, doi: [10.3390/app11020538](https://doi.org/10.3390/app11020538).
- [23] R.-J. Wai, M.-W. Chen, and J.-X. Yao, "Observer-based adaptive fuzzy-neural-network control for hybrid Maglev transportation system," *Neurocomputing*, vol. 175, pp. 10–24, Jan. 2016, doi: [10.1016/j.neucom.2015.10.006](https://doi.org/10.1016/j.neucom.2015.10.006).
- [24] C. Fu, J. Yu, L. Zhao, H. Yu, C. Lin, and Y. Ma, "Barrier Lyapunov function-based adaptive fuzzy control for induction motors with iron losses and full state constraints," *Neurocomputing*, vol. 287, pp. 208–220, Apr. 2018, doi: [10.1016/j.neucom.2018.02.020](https://doi.org/10.1016/j.neucom.2018.02.020).
- [25] D. Xu, J. Huang, X. Su, and P. Shi, "Adaptive command-filtered fuzzy backstepping control for linear induction motor with unknown end effect," *Inf. Sci.*, vol. 477, pp. 118–131, Mar. 2019, doi: [10.1016/j.ins.2018.10.032](https://doi.org/10.1016/j.ins.2018.10.032).
- [26] K. Saad, K. Abdellah, H. Ahmed, and A. Iqbal, "Investigation on SVM-backstepping sensorless control of five-phase open-end winding induction motor based on model reference adaptive system and parameter estimation," *Eng. Sci. Technol.*, vol. 22, pp. 1013–1026, Aug. 2019, doi: [10.1016/j.jestch.2019.02.008](https://doi.org/10.1016/j.jestch.2019.02.008).
- [27] L. Rincon, Y. Kubota, G. Venture, and Y. Tagawa, "Inverse dynamic control via 'simulation of feedback control' by artificial neural networks for a crane system," *Control Eng. Pract.*, vol. 94, Jan. 2020, Art. no. 104203, doi: [10.1016/j.conengprac.2019.104203](https://doi.org/10.1016/j.conengprac.2019.104203).
- [28] R. Salim, A. Mansouri, A. Bendiabdellah, S. Chekroun, and M. Touam, "Sensorless passivity based control for induction motor Via an adaptive observer," *ISA Trans.*, vol. 84, pp. 118–127, Jan. 2019, doi: [10.1016/j.isatra.2018.10.002](https://doi.org/10.1016/j.isatra.2018.10.002).
- [29] R. N. Mishra and K. B. Mohanty, "Development and implementation of induction motor drive using sliding-mode based simplified neuro-fuzzy control," *Eng. Appl. Artif. Intell.*, vol. 91, May 2020, Art. no. 103593, doi: [10.1016/j.engappai.2020.103593](https://doi.org/10.1016/j.engappai.2020.103593).
- [30] D. Fereka, M. Zerikat, and A. Belaidi, "MRAS sensorless speed control of an induction motor drive based on fuzzy sliding mode control," in *Proc. 7th Int. Conf. Syst. Control (ICSC)*, Valencia, Spain, 2018, pp. 230–236, Dec. 2018, doi: [10.1109/ICoSC.2018.8587844](https://doi.org/10.1109/ICoSC.2018.8587844).
- [31] E. A. De Freitas Nunes, A. O. Salazar, E. R. L. Villarreal, F. E. C. Souza, L. P. D. S. Júnior, J. S. B. Lopes, and J. C. C. Luque, "Proposal of a fuzzy controller for radial position in a bearingless induction motor," *IEEE Access*, vol. 7, pp. 114808–114816, Aug. 2019, doi: [10.1109/ACCESS.2019.2934820](https://doi.org/10.1109/ACCESS.2019.2934820).
- [32] N. Farah, M. H. N. Talib, and N. S. M. Shah, "A novel self-tuning fuzzy logic controller based induction motor drive system: An experimental approach," *IEEE Access*, vol. 7, pp. 68172–68184, May 2019, doi: [10.1109/ACCESS.2019.2916087](https://doi.org/10.1109/ACCESS.2019.2916087).
- [33] H. Mohan, M. K. Pathak, and S. K. Dwivedi, "Reactive power based speed control of induction motor drive using fuzzy logic for industrial applications," in *Proc. IEEE Int. Conf. Power Electron., Smart Grid Renew. Energy (PESGRE)*, Cochin, India, Jan. 2020, pp. 1–5, doi: [10.1109/PESGRE45664.2020.9070692](https://doi.org/10.1109/PESGRE45664.2020.9070692).
- [34] Z. Zhao, J. Yu, L. Zhao, H. Yu, and C. Lin, "Adaptive fuzzy control for induction motors stochastic nonlinear systems with input saturation based on command filtering," *Inf. Sci.*, vols. 463–464, pp. 186–195, Oct. 2018, doi: [10.1016/j.ins.2018.06.042](https://doi.org/10.1016/j.ins.2018.06.042).
- [35] X. Yang, J. Cui, D. Lao, D. Li, and J. Chen, "Input shaping enhanced active disturbance rejection control for a twin rotor multi-input multi-output system (TRMS)," *ISA Trans.*, vol. 62, pp. 287–298, May 2016, doi: [10.1016/j.isatra.2016.02.001](https://doi.org/10.1016/j.isatra.2016.02.001).



- [36] E. Omelchenko, T. Khrumshin, V. Tanich, and I. Kozhevnikov, "Dynamic computer model of traction asynchronous motor," in *Proc. IEEE Russian Workshop Power Eng. Autom. Metall. Ind. Res. Pract. (PEAMI)*, Magnitogorsk, Russia, Oct. 2019, pp. 59–63, doi: [10.1109/PEAMI.2019.8915408](https://doi.org/10.1109/PEAMI.2019.8915408).
- [37] C. M. Zhang, F. Lin, W. C. Song, and L. W. Jiao, "Nonlinear control of induction motors based on direct feedback linearization," *Proc. Chin. Soc. Elec. Eng.*, vol. 23, no. 2, pp. 99–107, Feb. 2003.
- [38] J. Q. Han, "Auto disturbance rejection controller and its applications," *Control Decis.*, vol. 13, no. 1, pp. 19–23, Jan. 1998, doi: [10.13195/j.cd.1998.01.19.hanjq.004](https://doi.org/10.13195/j.cd.1998.01.19.hanjq.004).
- [39] W.-H. Chen, J. Yang, L. Guo, and S. Li, "Disturbance-observer-based control and related methods—An overview," *IEEE Trans. Ind. Electron.*, vol. 63, no. 2, pp. 1083–1095, Feb. 2016, doi: [10.1109/TIE.2015.2478397](https://doi.org/10.1109/TIE.2015.2478397).
- [40] Z. H. Wu and B. Z. Guo, "Approximate decoupling and output tracking for MIMO nonlinear systems with mismatched uncertainties via ADRC approach," *J. Franklin Inst.*, vol. 355, no. 9, pp. 3873–3894, Jun. 2018, doi: [10.1016/j.jfranklin.2018.03.005](https://doi.org/10.1016/j.jfranklin.2018.03.005).
- [41] R. Patelski and D. Pazderski, "Improving the active disturbance rejection controller tracking quality by the input-gain underestimation for a second-order plant," *Electronics*, vol. 10, no. 8, pp. 1–16, Apr. 2021, doi: [10.3390/electronics10080907](https://doi.org/10.3390/electronics10080907).
- [42] M. P. Ran, Q. Wang, C. Y. Dong, and L. H. Xie, "Active disturbance rejection control for uncertain time-delay nonlinear systems," *Automatica*, vol. 112, Feb. 2020, Art. no. 108692, doi: [10.1016/j.automatica.2019.108692](https://doi.org/10.1016/j.automatica.2019.108692).
- [43] L. Sun, Y. H. Jin, and F. Q. You, "Active disturbance rejection temperature control of open-cathode proton exchange membrane fuel cell," *Appl. Energy*, vol. 261, pp. 1–13, Mar. 2020, doi: [10.1016/j.apenergy.2019.114381](https://doi.org/10.1016/j.apenergy.2019.114381).
- [44] F. Deng and Y. Guan, "PMSM vector control based on improved ADRC," in *Proc. IEEE Int. Conf. Intell. Robotic Control Eng. (IRCE)*, Lanzhou, China, Aug. 2018, pp. 154–158, doi: [10.1109/IRCE.2018.8492927](https://doi.org/10.1109/IRCE.2018.8492927).
- [45] R. Patelski and P. Dutkiewicz, "On the stability of ADRC for manipulators with modelling uncertainties," *ISA Trans.*, vol. 102, pp. 295–303, Jul. 2020, doi: [10.1016/j.isatra.2020.02.027](https://doi.org/10.1016/j.isatra.2020.02.027).
- [46] S. Zhonghua, "Design and simulation of naval gun servo controller based on ADRC," in *Proc. 11th Int. Conf. Measuring Technol. Mechatronics Autom. (ICMTMA)*, Qiqihar, China, Apr. 2019, pp. 345–349, doi: [10.1109/ICMTMA.2019.00083](https://doi.org/10.1109/ICMTMA.2019.00083).
- [47] Z. J. Huang, Y. J. Liu, H. Zheng, and S. T. Wang, "A self-searching optimal ADRC for the pitch angle control of an underwater thermal glider in the vertical plane motion," *Ocean Eng.*, vol. 159, pp. 98–111, Jul. 2018, doi: [10.1016/j.oceaneng.2018.04.010](https://doi.org/10.1016/j.oceaneng.2018.04.010).
- [48] F. Xie, W. Hong, and C. Qiu, "Speed fluctuation suppression of PMSM using active disturbance rejection and feedback compensation control," *IET Electr. Power Appl.*, pp. 1–12, Mar. 2021, doi: [10.1049/elp2.12079](https://doi.org/10.1049/elp2.12079).
- [49] M. A. Lotufo, L. Colangelo, P. M. Carlos, and E. Canuto, "UAV quadrotor attitude control: An ADRC-EMC combined approach," *Control Eng. Pract.*, vol. 84, pp. 13–22, Mar. 2019, doi: [10.1016/j.conengprac.2018.11.002](https://doi.org/10.1016/j.conengprac.2018.11.002).
- [50] R. Li, B. Jia, S. Fan, and X. Pan, "A novel active disturbance rejection control with hyperbolic tangent function for path following of underactuated marine surface ships," *Meas. Control*, vol. 53, nos. 9–10, pp. 1579–1588, Nov. 2020, doi: [10.1177/0020294020952484](https://doi.org/10.1177/0020294020952484).
- [51] L. Y. Si, W. P. Cao, and X. P. Chen, "Active disturbance rejection control of a longitudinal tunnel ventilation system," *Energies*, vol. 13, no. 8, pp. 1–16, Apr. 2020, doi: [10.3390/en13081871](https://doi.org/10.3390/en13081871).
- [52] X. Y. Cao, W. Z. Wang, and X. G. Zhang, "Precise locating control for a polar crane based on sliding mode active disturbance rejection control and quadratic programming algorithm," *Machines*, vol. 9, no. 2, pp. 1–21, Feb. 2021, doi: [10.3390/machines9020022](https://doi.org/10.3390/machines9020022).
- [53] I. Ferdiansyah, L. P. S. Raharja, D. S. Yanaratri, and E. Purwanto, "Design of PID controllers for speed control of three phase induction motor based on direct-axis current (Id) coordinate using IFOC," in *Proc. 4th Int. Conf. Inf. Technol., Inf. Syst. Electr. Eng. (ICITISEE)*, Nov. 2019, pp. 369–372, doi: [10.1109/ICITISEE48480.2019.9003893](https://doi.org/10.1109/ICITISEE48480.2019.9003893).



**ZHONG BIN** was born in Sichuan, China, in 1975. He received the B.E. and M.E. degrees in mechanical engineering from the College of Engineering and Technology (CET), Southwest University, Chongqing, China, in 2000 and 2005, respectively, and the Ph.D. degree in mechatronic engineering from the School of Mechanical Engineering, Southwest Jiaotong University, Chengdu, China, in 2007. He currently serves as a Professor and a Doctoral Supervisor with the School of Mechanical Engineering, Chengdu University, Sichuan. His research interests include mechatronics, motion control, and intelligent robotic system applications.



**MA LILI** was born in Jiangsu, China, in 1980. She received the B.E. and M.E. degrees in mechanical engineering from the College of Engineering and Technology (CET), Southwest University, Chongqing, China, in 2002 and 2005, respectively, and the Ph.D. degree in mechatronic engineering from the School of Mechanical Engineering, Southwest Jiaotong University, Chengdu, China, in 2013. She currently serves as a Lecturer with the College of Equipment Management and Support, Engineering University of PAP. Her research interests include mechatronics, computer vision, and intelligent robots.



**DONG HAO** received the B.E. and Ph.D. degrees in mechanical engineering from the School of Mechanical Engineering, Southwest Jiaotong University, Chengdu, China, in 2008 and 2015, respectively. He currently serves as an Associate Researcher with the School of Mechanical Engineering, Chengdu University. He is a member of the Chinese Society of Mechanics.



**REN ZHENXING** was born in Sichuan, China, in 1979. He received the B.E. degree in mechanical engineering and the M.E. degree in measuring and testing technologies and instruments from the School of Mechanical Engineering, Southwest Petroleum University, Chengdu, China, in 2002 and 2005, respectively, and the Ph.D. degree in physical electronics from the Institute of Electronics, Chinese Academy of Sciences, Beijing, China, in 2011. He currently serves as an Associate Professor with the School of Mechanical Engineering, Chengdu University, Sichuan. His research interests include sensor technology, motion control, and intelligent robotic system applications.

...